2016

Structural health monitoring ultrasonic thickness measurement accuracy and reliability of various time-of-flight calculation methods

Thomas J. Eason
Iowa State University and BP Products North America

Leonard J. Bond
Iowa State University, bondlj@iastate.edu

Mark G. Lozev
BP Products North America

Structural health monitoring ultrasonic thickness measurement accuracy and reliability of various time-of-flight calculation methods

Abstract

The accuracy, precision, and reliability of ultrasonic thickness structural health monitoring systems are discussed in-cluding the influence of systematic and environmental factors. To quantify some of these factors, a compression wave ultrasonic thickness structural health monitoring experiment is conducted on a flat calibration block at ambient temperature with forty four thin-film sol-gel transducers and various time-of-flight thickness calculation methods. As an initial calibration, the voltage response signals from each sensor are used to determine the common material velocity as well as the signal offset unique to each calculation method. Next, the measurement precision of the thickness error of each method is determined with a proposed weighted censored relative maximum likelihood analysis technique incorporating the propagation of asymmetric measurement uncertainty. The results are presented as upper and lower confidence limits analogous to the *a*90/95 terminology used in industry recognized Probability-of-Detection assessments. Future work is proposed to apply the statistical analysis technique to quantify measurement precision of various thickness calculation methods under different environmental conditions such as high temperature, rough back-wall surface, and system degradation with an intended application to monitor naphthenic acid corrosion in oil refineries.

Keywords

Ultrasonics, Wave mechanics, Industry, Corrosion, Solgels, Thin films

Disciplines

Mechanics of Materials | Structures and Materials

Structural health monitoring ultrasonic thickness measurement accuracy and reliability of various time-of-flight calculation methods

Cite as: AIP Conference Proceedings **1706**, 200003 (2016); https://doi.org/10.1063/1.4940647
Published Online: 10 February 2016

Thomas J. Eason, Leonard J. Bond, and Mark G. Lozev

Structural Health Monitoring Ultrasonic Thickness Measurement Accuracy and Reliability of Various Time-of-Flight Calculation Methods

Thomas J. Eason[1,2,a)], Leonard J. Bond[1] and Mark G. Lozev[2]

[1]*Center for Nondestructive Evaluation, Iowa State University, 1915 Scholl Rd., Ames, IA*
[2]*BP Products North America, Refining and Logistics Technology, 150 W. Warrenville Rd., Naperville, IL*

[a)]easont@iastate.edu

Abstract. The accuracy, precision, and reliability of ultrasonic thickness structural health monitoring systems are discussed in-cluding the influence of systematic and environmental factors. To quantify some of these factors, a compression wave ultrasonic thickness structural health monitoring experiment is conducted on a flat calibration block at ambient temperature with forty four thin-film sol-gel transducers and various time-of-flight thickness calculation methods. As an initial calibration, the voltage response signals from each sensor are used to determine the common material velocity as well as the signal offset unique to each calculation method. Next, the measurement precision of the thickness error of each method is determined with a proposed weighted censored relative maximum likelihood analysis technique incorporating the propagation of asymmetric measurement uncertainty. The results are presented as upper and lower confidence limits analogous to the $a_{90/95}$ terminology used in industry recognized Probability-of-Detection assessments. Future work is proposed to apply the statistical analysis technique to quantify measurement precision of various thickness calculation methods under different environmental conditions such as high temperature, rough back-wall surface, and system degradation with an intended application to monitor naphthenic acid corrosion in oil refineries.

INTRODUCTION

The changing world supply of crude oil towards properties of higher density, higher sulfur concentration, and higher acidity can result in additional fuel production challenges for oil refineries [1, 2]. One such production challenge is an increased risk of naphthenic acid corrosion that can result in various surface degradation profiles of uniform corrosion, non-uniform corrosion, and localized pitting in piping systems at temperatures between 150°C and 400°C [3, 4]. The accuracy, precision, and reliability of structural health monitoring thickness measurement systems must be sufficient to provide a better understanding of the integrity risk associated with refining crude oils of higher acid concentration. It is prudent to first establish a method to statistically quantify the measurement uncertainty, then apply the method to a significant number of sensors in a baseline scenario on a smooth surface at ambient temperature before taking measurements in more extreme environments at elevated temperatures, for rough back-wall surfaces, and for system degradation over time. This paper addresses sources of uncertainty in structural health monitoring ultrasonic thickness measurements, proposes a weighted censored relative likelihood analysis method to capture asymmetric measurement uncertainty, and demonstrates the method using sol-gel transducers [5, 6, 7] in calibration of the measurement system and in establishing the baseline thickness measurement error accuracy and precision for a number of relatively simple time-of-flight thickness calculation methods.

BACKGROUND

Ultrasonic Thickness Measurement

A bulk wave ultrasonic thickness measurement technique for corrosion monitoring can be applied with temporary or permanent coupling of a transducer to the outside surface of a pipe; the pipe wall thickness can be determined

42nd Annual Review of Progress in Quantitative Nondestructive Evaluation
AIP Conf. Proc. 1706, 200003-1–200003-11; doi: 10.1063/1.4940647

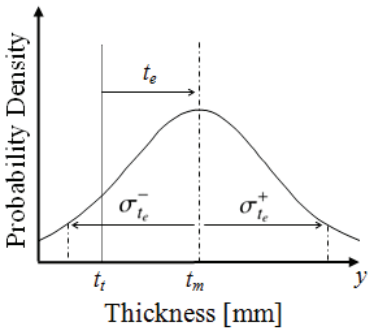

FIGURE 1. Thickness measurement Probability Density Function to demonstrate measurement accuracy represented as a thickness error t_e, and measurement precision represented as positive and thickness error$_t$ uncertainty$_t$ σ^+_e and σ^+_e. The thickness error t_e can be positive or negative defined as the difference between measured thickness t_m and true thickness t_t.

from the time difference in transducer excitation and reception of the reflected wave from the back-wall surface [8, 9, 10, 11].

The measured thickness t_m is related to the bulk longitudinal wave speed c and the time-of-flight of a feature from the first back-wall reflection for pulse-echo (single transducer) τ_{1PE} and pitch-catch (two transducers) τ_{1PC} configurations as shown in Eq. 1 where τ_o is a time offset and x_p is the center distance (pitch) between the two transducers neglecting pipe curvature. The wave speed c and time offset τ_o can be specified during initial calibration. The offset time is not necessary when multiple reflections are present on a calibration block, but multiple reflections may not be present with a rough back-wall surface as a result of internal pipe corrosion [8].

$$t_m = \frac{c\,(\tau_{1PE} - \tau_o)}{2} \qquad t_m = \sqrt{\left(\frac{c\,(\tau_{1PC} - \tau_o)}{2}\right)^2 - \left(\frac{x_p}{2}\right)^2} \tag{1}$$

Structural Health Monitoring Ultrasonic Thickness Measurement Uncertainty

Measurement uncertainty for permanently installed, fixed, structural health monitoring ultrasonic thickness measurement systems can be categorized as follows: accuracy of a single sensor measurement, precision among multiple measurements of a single sensor, precision of a single measurement among multiple sensors, and reliability of measurements over time. The accuracy of a single sensor measurement can be influenced by the sampling rate, transducer bandwidth, excitation frequency, time-of-flight calculation method [12], as well as the velocity, offset, and temperature calibration. The precision among multiple measurements of a single sensor (over a short time period) can be described as measurement repetition uncertainty and can be influenced by system stability. The precision of a single measurement among multiple sensors (over a short time period) can be described as spatial variation among an array of sensors and can be influenced by sensor fabrication consistency, coupling consistency, acoustic velocity material variation (caused by spatial temperature variation), and variation in the back-wall surface roughness [13, 14]. The reliability of a single (or multiple) measurement(s) from a single (or array) of sensors can be described as temporal variation and can be influenced by piezoelectric aging, coupling degradation, electronics and cabling degradation, changing back-wall surface morphology, and acoustic velocity temporal variation (caused by temporal temperature variation). Other factors can also influence measurement uncertainty such as pulse-echo or pith-catch configuration, supply voltage, pipe geometry curvature, and the presence of a tapered back-wall [8].

Only the following accuracy and precision sources of uncertainty are quantified in this paper by comparing measurements with known true thickness reference values (over a short time period): sampling rate, time-of-flight calculation method, velocity and offset calibration, measurement repetition, and fabrication and coupling consistency.

Ultrasonic Thickness Measurement Error

The thickness measurement error for a pulse-echo configuration t_e is analogous to measurement accuracy as presented in Fig. 1 and is defined in Eq. 2 as the difference in measured thickness t_m and true thickness t_t. The

uncertainty of the thickness measurement error σ_{t_e} is analogous to measurement precision as presented in Fig 1 and defined in Eq. 2 with σ_c as the velocity uncertainty, σ_{τ_o} as the time offset uncertainty, σ_{t_t} as the true thickness dimensional uncertainty, and σ_{τ_1} as the time-of-flight measurement uncertainty. The measurement error uncertainty σ_{t_e} in Eq. 2 is determined by propagation of uncertainty [15] while assuming correlation among terms is secondary such that covariance is neglected. A positive thickness measurement error $\sigma^+_{t_e}$ indicates a measured thickness greater than the true thickness; a negative thickness measurement error $\sigma^-_{t_e}$ indicates a measured thickness less than the true thickness. The consequence of a positive or negative thickness measurement error is not the same in a corrosion monitoring application; therefore, measurement error asymmetry is of interest.

$$t_e = \frac{c\,(\tau_1 - \tau_o)}{2} - t_t \qquad \sigma^{\pm}_{t_e} = \sqrt{\frac{(\tau_1 - \tau_o)^2\,\sigma^{\pm 2}_c}{4} + \frac{c^2\left(\sigma^{\pm\,2}_{\tau_1} + \sigma^{\mp\,2}_{\tau_o}\right)}{4} + \sigma^{\mp 2}_{t_t}} \tag{2}$$

Uncertainty Analysis

The uncertainty components in Eq. 2 can be described as either Type B, the intrinsic measurement resolution limit, or as Type A, the natural variation that is present among a set of measurements [16]. Type A uncertainty can be modeled with location scale-distributions. Type B uncertainty can be incorporated into such distribution models with a censored relative likelihood analysis method described in this section.

Location-Scale Distributions

The probability density functions ϕ and cumulative distribution functions Φ of the Smallest Extreme Value (SEV), Largest Extreme Value (LEV), and Logistic (LGS) distributions are shown in Eqs. 3-5 with $z = \frac{y-\mu}{\sigma}$ as the normalized dispersion factor with y as an individual measured value, μ as the mean, and σ as the standard deviation [17]. The left-skewed (SEV), right-skewed (LEV), and symmetric (LGS) distributions have closed form cumulative distribution functions that allow for a relatively efficient computation as compared with the Normal distribution.

$$\phi_{SEV} = e^{(z-e^z)} \qquad \Phi_{SEV} = 1 - e^{(-e^z)} \tag{3}$$

$$\phi_{LEV} = e^{\left(-z-e^{-z}\right)} \qquad \Phi_{LEV} = e^{\left(-e^{-z}\right)} \tag{4}$$

$$\phi_{LGS} = \frac{e^z}{(1+e^z)^2} \qquad \Phi_{LGS} = \frac{e^z}{(1+e^z)} \tag{5}$$

Relative Likelihood

The industry standard for NDE reliability assessments [18] applies a relative likelihood method to quantify measurement error uncertainty for various location-scale distribution models. The likelihood L of a particular set of mean μ and deviation σ parameters is shown in Eq. 6 as the product of the probability density f of each individual measurement y for n total measurements. A range of μ and σ parameters are analyzed with the resulting maximum likelihood value corresponding to $\hat{\mu}$ and $\hat{\sigma}$. The relative likelihood R is a normalization of the maximum likelihood as shown in Eq. 7. A confidence region of the most likely μ and σ parameters corresponding to the relative likelihood values greater than α as derived from a χ^2 distribution with two degrees of freedom is shown in Eq. 8 [17]. The industry recognized a_{90} confidence value can be determined as the cumulative distribution point from the maximum likelihood $\hat{\mu}$ and $\hat{\sigma}$ model, while the $a_{90/95}$ confidence value can be determined with the Delta method to establish Wald confidence intervals [18]; alternatively, the $a_{90/95}$ confidence value can be determined using a simulation method to construct a set of distribution models with the μ and σ parameters from the relative likelihood confidence region perimeter [19].

$$L\,(\mu,\sigma) = \prod_{i=1}^{n} f\,(y_i;\mu,\sigma) = \prod_{i=1}^{n}\left[\tfrac{1}{\sigma}\phi\left(\tfrac{y_i-\mu}{\sigma}\right)\right] \tag{6}$$

$$R\,(\mu,\sigma) = \tfrac{L(\mu,\sigma)}{L(\hat{\mu},\hat{\sigma})} \tag{7}$$

$$R\,(\mu,\sigma) > \exp\left(\tfrac{-\chi^2_{(1-\alpha;2)}}{2}\right) = \alpha \tag{8}$$

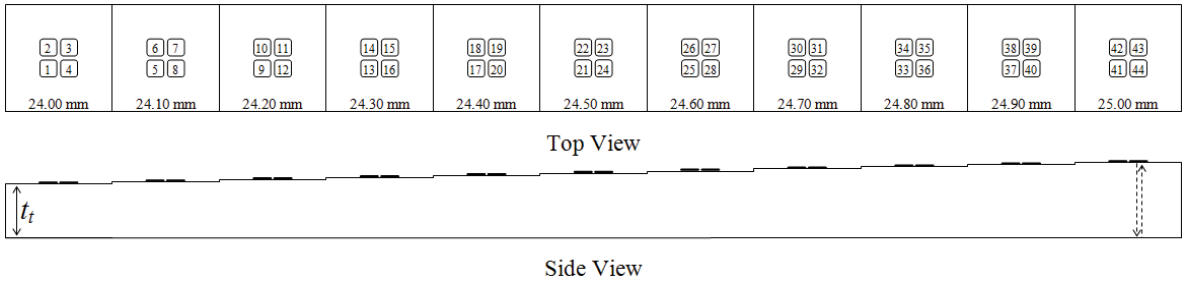

FIGURE 2. AISI 1018 carbon steel eleven step calibration block from 24.00 mm to 25.00 mm with 44 direct sol-gel transducers.

Censored Relative Likelihood

Instead of assuming a single point value for each measurement, the censored relative likelihood method uses an upper y_U and lower y_L confidence interval for each measurement as shown in Eq. 9 with F as the cumulative distribution function. The censored likelihood method has been previously applied for the normal distribution [20] and extreme value distributions [21] to account for measurement resolution and round-off error uncertainties.

$$L(\mu,\sigma) = \prod_{i=1}^{n} \left[F\left(y_{U_i};\mu,\sigma\right) - F\left(y_{L_i};\mu,\sigma\right)\right] = \prod_{i=1}^{n} \left[\Phi\left(\frac{y_{U_i}-\mu}{\sigma}\right) - \Phi\left(\frac{y_{L_i}-\mu}{\sigma}\right)\right] \tag{9}$$

Weighted Censored Relative Likelihood

The relative likelihood method does not capture an individual measurement data point confidence interval, and the censored relatively likelihood method does not consider if an individual measurement data point mean has asymmetric uncertainty. However, the individual data point mean and asymmetric measurement confidence intervals are considered in the proposed weighted censored relative likelihood method as described in Eq. 10 with κ as the weight parameter ranging from $\kappa = 0$ for no censoring (same as Eq. 6) to $\kappa = 1$ for full censoring (same as Eq. 9).

$$L(\mu,\sigma) = \prod_{i=1}^{n} \left[(1-\kappa)\, f\left(y_i\right) + \frac{\kappa}{2}\left[F\left(y_{U_i}\right) - F\left(y_{L_i}\right)\right]\right] = \prod_{i=1}^{n} \left[\frac{1-\kappa}{\sigma}\phi\left(\frac{y_i-\mu}{\sigma}\right) + \frac{\kappa}{2}\left[\Phi\left(\frac{y_{U_i}-\mu}{\sigma}\right) - \Phi\left(\frac{y_{L_i}-\mu}{\sigma}\right)\right]\right] \tag{10}$$

Applied Likelihood Method

The applied likelihood uncertainty analysis method is described. First, the weighted ($\kappa = 0.5$) censored maximum likelihood SEV, LEV, or LGS location-scale distribution model is identified to generate a confidence region ($\alpha = .05$) from the corresponding relative likelihood function. Then, a new set of potential distribution models are simulated from the μ and σ parameters on the confidence region perimeter. Finally, the most likely mean $\hat{\mu}$ from the maximum likelihood distribution is considered the most likely mean term $\overline{y} = \hat{\mu}$, and, the 95% upper and 5% lower confidence limits from the set of simulated distribution models $a_{95/95}$ and $a_{05/05}$ are used to determine the (possibly asymmetric) upper uncertainty $\sigma_{\overline{y}}^{+} = a_{95/95} - \overline{y}$ and lower uncertainty $\sigma_{\overline{y}}^{-} = \overline{y} - a_{05/05}$. This method is applied three times in course of determining thickness error uncertainty: velocity calibration, offset calibration, and thickness error. A demonstration of the method can be observed in Figs. 4-6.

METHODOLOGY

Experiment Setup

A total of forty four sol-gel sensor element transducers [5, 6, 7] were directly deposited in 2 x 2 array groups onto a flat step calibration block with a 0.10 ± 0.005 mm step size from 24.00 mm to 25.00 mm as shown in Fig. 2 and previously described [19, 22]. The gain for each sensor was individually adjusted to maximize the first back-wall reflection amplitude without saturation. A total of 44 pulse-echo waveforms were collected for each of the sensor elements over a period of 90 minutes at constant indoor ambient temperature resulting in 1936 individual voltage

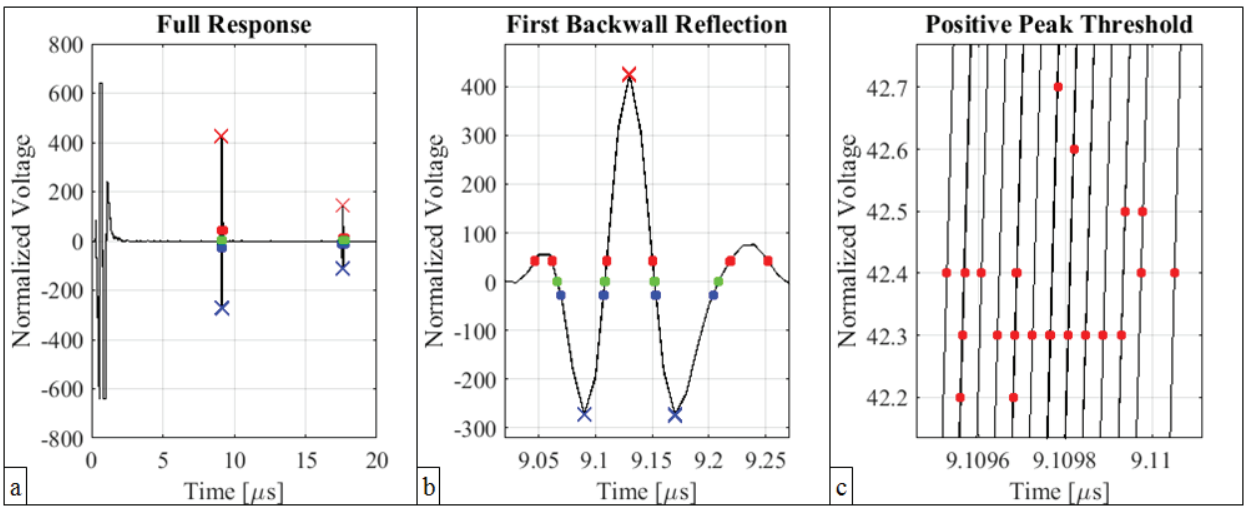

FIGURE 3. Overlay plots of 44 voltage response signals from a single sensor for a) the full response, b) a close view of the first back-wall reflection, and c) a very close view of the positive peak threshold features. The various features are observable as positive peak [×], 10% positive threshold [•], 10% zero-crossing [•], 10% negative threshold [•], and negative peak [×].

response signals. The elements have a center frequency from 6.9 MHz to 9.1 MHz and a bandwidth from 72% to 79% at -6 dB. One sensor did not produce a response signal and was excluded from the analysis as an outlier.

Time-of-Flight Calculation Methods

While many different thickness calculation methods exist [23], this paper addresses relatively simple time-of-flight methods; the initial focus is not to discover the most precise method, but rather, avoid the least precise among commonly used methods. A total of 87 time-of-flight measurement methods were investigated as described in Table 1 based on the voltage amplitude and arrival time of various signal features within a time gate region around the first (and sometimes second) back-wall reflection. The positive, negative, and zero-crossing voltage measurement refers to features at a positive, negative, or zero voltage. The rectified voltage measurement refers to features of a rectified voltage signal. The voltage threshold refers to features at a positive (or negative) voltage as a percentage of the maximum (or minimum) peak voltage. The peak category refers to features at the maximum (or minimum) voltage. The first threshold category refers to the first feature on a voltage threshold. The mean threshold category refers to the mean of features on a voltage threshold. The peak threshold category refers to the feature on a voltage threshold immediately preceding a maximum (or minimum) peak feature.

TABLE 1. Description of 87 time-of-flight measurement method combinations.

Voltage Measurement	Voltage Threshold	Category
Positive	75%	Peak*
Negative	50%	Threshold - First
Zero-Crossing	25%	Threshold - Mean
Rectified	20%	Threshold - Peak
	15%	
	10%	
	5%	

* Peak is excluded among the other 84 category combinations. Peak describes only 3 methods for positive, negative, and rectified voltage.

Overlay plots of all 44 voltage response signals from a single sensor are shown in Fig. 3. Features are identified within gated regions around the first and second back-wall reflections; slight variation of a feature is observable in Fig. 3c as repetition uncertainty.

Considered Uncertainty Factors

This section details the error propagation and likelihood methods applied to quantify the uncertainty components in Eq. 2. A variable with a j subscript indicates uniqueness to a particular calculation method; a k subscript indicates uniqueness to a particular sensor; an l subscript indicates uniqueness to a particular response signal; no subscript indicates applicability among all calculation methods, sensors, and response signals. The typical absolute and relative uncertainty values are summarized in Table 2.

TABLE 2. Average negative and positive uncertainty range of factors for peak and threshold calculation methods.

Factors		**Average Uncertainty Range**			
Name	Symbol	Peak Methods		Threshold Methods	
True Thickness	$\sigma_{t_t k}$	-.005mm – .005mm	-.02% – .02%	-.005mm – .005mm	-.02% – .02%
Sound Path	$\sigma_{d_{PE}k}$	-.010mm – .010mm	-.02% – .02%	-.010mm – .010mm	-.02% – .02%
Repetition	$\sigma_{R_{2-1}jk}$	-0.2ns – 0.2ns	-.002% – .002%	-0.8ns – 0.8ns	-.01% – .01%
Sampling	$\sigma_{S_{2-1}jk}$	-10ns – 10ns	-0.1% – 0.1%	~ 0ns	~ 0%
Feature Arrival	$\sigma_{\tau_{2-1}jk}$	-10ns – 10ns	-0.1% – 0.1%	-0.8ns – 0.8ns	-.01% – .01%
Velocity	σ_{cjk}	-7m/s – 7m/s	-0.1% – 0.1%	-2m/s – 2m/s	-.03% – .03%
Velocity*	σ_{cj}	-41m/s – 16m/s	-0.7% – 0.3%	-48m/s – 26m/s	-0.8% – 0.4%
Repetition	$\sigma_{R_1 jk}$	-0.1ns – 0.1ns	-.001% – .001%	-0.4ns – 0.4ns	-.004% – .004%
Sampling	$\sigma_{S_1 jk}$	-5ns – 5ns	-.06% – .06%	~ 0ns	~ 0%
Feature Arrival	$\sigma_{\tau_1 jk}$	-5ns – 5ns	-.06% – .06%	-0.4ns – 0.4ns	-.004% – .004%
Offset	$\sigma_{\tau_o jk}$	-11ns – 7ns	-1.6% – 1.0%	-10ns – 5ns	-1.5% – 0.7%
Offset*	$\sigma_{\tau_o j}$	-59ns – 55ns	-8.5% – 8.1%	-42ns – 66ns	-6.2% – 9.5%
Thickness	$\sigma_{t_m jk}$	-0.2mm – 0.2mm	-0.7% – 0.7%	-0.2mm – 0.1mm	-0.8% – 0.5%
Thickness Error†	$\sigma_{t_e jk}$	-0.2mm – 0.2mm	n/a	-0.2mm – 0.1mm	n/a
Thickness Error*†	$\sigma_{t_e j}$	-0.2mm – 0.2mm	n/a	-0.1mm – 0.2mm	n/a

* Average uncertainty ranges are from weighted censored relative likelihood method analysis for average negative uncertainty from $a_{05/05}$ and positive uncertainty from $a_{95/95}$ among different calculation methods.
† Average uncertainty ranges are different than the Thickness uncertainty range beyond the reported significant digits.

Repetition, Sampling Rate, and Dimensional Uncertainty

For each of the 87 calculation method, and each of the 43 sensors, and each of the 44 voltage response signals, the feature arrival point of the first back-wall reflection $\tau_{1\,jkl}$ and the feature arrival point difference between the second and first back-wall reflections $\tau_{2-1\,jkl}$ were captured. These feature arrival points were re-converted to time units by dividing the digitized points by the sampling rate of 100 MHz. The mean feature arrival times $\tau_{1\,jk}$ and $\tau_{2-1\,jk}$ of the 44 voltage response signals were captured along with the corresponding standard errors $\mathrm{SE}_{\tau_1\,jk}$ and $\mathrm{SE}_{\tau_{2-1}\,jk}$.

The measurement repetition uncertainty $\sigma^{\pm}_{R\,jk}$ of a mean feature arrival time τ_{jk} is considered Type A and can be approximated by a t-distribution with $\alpha = 0.05$ and 43 degrees of freedom [16] as symmetric uncertainty $\sigma^{\pm}_{R\,jk} = t_{(0.95,43)}\mathrm{SE}_{\tau\,jk}\sqrt{43} = 2.0168 \cdot \mathrm{SE}_{\tau\,jk}\sqrt{43}$.

The sampling rate uncertainty $\sigma^{\pm}_{S\,j}$ of any mean feature is considered Type B for only the three peak calculation methods. For a single feature, the symmetric uncertainty $\sigma^{\pm}_{S_1\,j} = 5$ ns; for the difference in two features, the symmetric uncertainty $\sigma^{\pm}_{S_{2-1}\,j} = 10$ ns. For the non-peak methods, the sampling rate uncertainty $\sigma^{\pm}_{S\,j} \approx 0$ ns as such methods are linearly interpolated between two points and the linear interpolation error << 1 ns.

The true thickness t_{tk} of the calibration block ranges from 24.00 to 25.00 mm with a corresponding Type B symmetric uncertainty fabrication tolerance $\sigma^{\pm}_{t_t\,k} = 0.005$ mm. In pulse echo mode, the sound path distance $d_{PE\,k} = 2{\cdot}t_{tk}$ ranges from 48.00 to 50.00 mm with a corresponding symmetric uncertainty $\sigma^{\pm}_{d_{PE}\,k} = 2 \cdot \sigma^{\pm}_{t_t\,k} = 0.01$ mm.

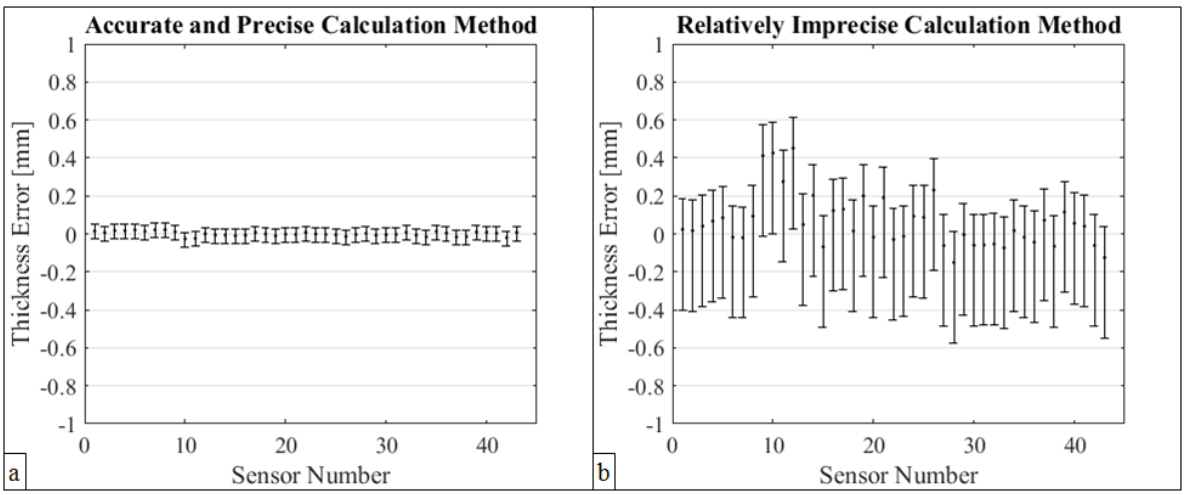

FIGURE 4. The thickness error calculation from the same voltage response signals for each of the 43 sensors are shown for a) an accurate and precise calculation method and b) a relatively imprecise calculation method.

Velocity Uncertainty

The common material velocity c can be borrowed from a reference [24] or directly measured. The measured material velocity c_{jk} and associated uncertainty $\sigma^{\pm}_{c\,jk}$ are described in Eq. 11 where $\sigma^{\mp}_{\tau_{2-1}\,jk} = \sigma^{\mp}_{R_{2-1}\,jk} + \sigma^{\mp}_{S_{2-1}\,j}$. These terms are input to the previously described likelihood method with $y_i = c_{jk}$, $y_U = c_{jk} + \sigma^{+}_{c\,jk}$, and $y_L = c_{jk} - \sigma^{-}_{c\,jk}$ to generate the most likely material velocity c_j, positive uncertainty $\sigma^{+}_{c\,j}$, and negative uncertainty $\sigma^{-}_{c\,j}$ for each of the 87 calculation methods. The method with the smallest uncertainty range $(\sigma^{+}_{c\,j} - \sigma^{-}_{c\,j})$ was selected such that $c = 5909.9$m/s, $\sigma^{+}_{c} = 7.1$m/s, and $\sigma^{-}_{c} = 2.9$m/s as the common material velocity and velocity uncertainty.

$$c_{jk} = \frac{d_{PEk}}{\tau_{2-1\,jk}} \qquad \sigma^{\pm}_{c\,jk} = c_{jk}\sqrt{\left(\frac{\sigma^{\pm}_{d_{PE}k}}{d_{PEk}}\right)^2 + \left(\frac{\sigma^{\mp}_{\tau_{2-1}\,jk}}{\tau_{2-1\,jk}}\right)^2} \tag{11}$$

Offset Uncertainty

The response signal offset time $\tau_{o\,j}$ is to compensate for the slight difference among feature locations unique to each calculation method when considering only the first back-wall reflection. The offset time $\tau_{o\,j}$ is different, and much smaller, than a delay time that would need to be considered for any probe design without direct contact between the piezoelectric material and pipe surface. The measured offset time $\tau_{o\,jk}$ and associated uncertainty $\sigma^{\pm}_{\tau_o\,jk}$ are described in Eq. 12 where $\sigma^{\pm}_{\tau_1\,jk} = \sigma^{\pm}_{R_1\,jk} + \sigma^{\pm}_{S_1\,j}$. These terms are input to the previously described likelihood method with with $y_i = \tau_{o\,jk}$, $y_U = \tau_{o\,jk} + \sigma^{+}_{\tau_o\,jk}$, and $y_L = \tau_{o\,jk} - \sigma^{-}_{\tau_o\,jk}$ to generate the most likely offset time $\tau_{o\,j}$, positive uncertainty $\sigma^{+}_{\tau_o\,j}$, and negative uncertainty $\sigma^{-}_{\tau_o\,j}$ for each of the 87 calculation methods.

$$\tau_{o\,jk} = \tau_{1\,jk} - \frac{d_{PEk}}{c} \qquad \sigma^{\pm}_{\tau_o\,jk} = \sqrt{{\sigma^{\pm}_{\tau_1\,jk}}^2 + \left(\frac{d_{PEk}}{c}\right)^2\left[\left(\frac{\sigma^{\mp}_{d_{PE}k}}{d_{PEk}}\right)^2 + \left(\frac{\sigma^{\pm}_{c}}{c}\right)^2\right]} \tag{12}$$

Thickness Measurement Uncertainty

The thickness measurement $t_{m\,jk}$ and associated uncertainty $\sigma^{\pm}_{t_m\,jk}$ are described in Eq. 13. The thickness measurement uncertainty $\sigma_{t_m\,j}$ provides an indication of measurement precision for each calculation method.

$$t_{m\,jk} = \frac{c\left(\tau_{1\,jk} - \tau_{o\,j}\right)}{2} \qquad \sigma^{\pm}_{t_m\,jk} = \frac{1}{2}\sqrt{\left(\tau_{1\,jk} - \tau_{o\,j}\right)^2 \sigma^{\pm 2}_{c} + c^2\left({\sigma^{\pm}_{\tau_1\,jk}}^2 + {\sigma^{\mp}_{\tau_o\,j}}^2\right)} \tag{13}$$

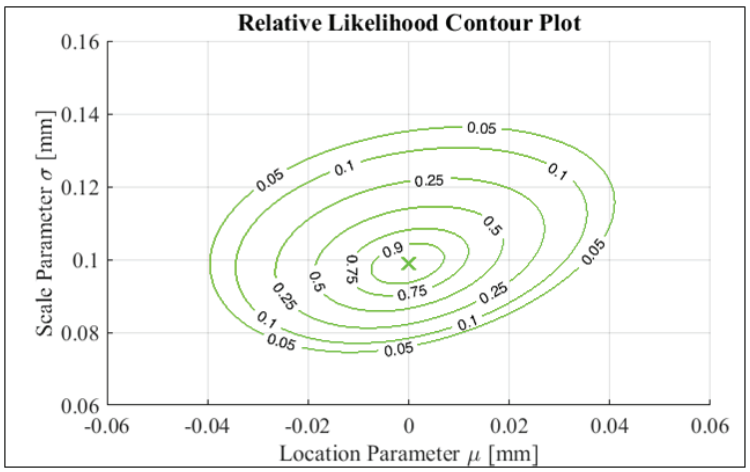

FIGURE 5. The relative likelihood contour plot for the relatively imprecise measurement method is shown. The 95% confidence region perimeter can be taken as the set of location scale parameters μ and σ on the 0.05 contour line.

Thickness Measurement Error Uncertainty

The thickness measurement error $t_{e\,jk}$ and associated uncertainty $\sigma^{\pm}_{t_e\,jk}$ are described in Eq. 14. These terms are input to the previously described likelihood method with $y_i = t_{e\,jk}$, $y_U = t_{e\,jk} + \sigma^{+}_{t_e\,jk}$, and $y_L = t_{e\,jk} - \sigma^{-}_{t_e\,jk}$ to generate the most likely thickness measurement error $t_{e\,j}$, positive uncertainty $\sigma^{+}_{t_e\,j}$, and negative uncertainty $\sigma^{-}_{t_e\,j}$ for each of the 87 calculation methods. These values provide an indication of measurement accuracy and precision for each calculation method. The 95% upper confidence limit from the set of simulated distribution models $a_{95/95\,j} = t_{e\,j} + \sigma^{+}_{t_e\,j}$ is of most interest. This upper confidence limit represents the largest expected measurement error corresponding to a measured thickness greater than the true thickness, and described as an over-reporting of the thickness.

$$t_{e\,jk} = \frac{c\left(\tau_{1\,jk} - \tau_{o\,j}\right)}{2} - t_{tk} \qquad \sigma^{\pm}_{t_e\,jk} = \sqrt{\frac{\left(\tau_{1\,jk} - \tau_{o\,j}\right)^2 \sigma^{\pm 2}_{c}}{4} + \frac{c^2\left(\sigma^{\pm}_{\tau_1\,jk}{}^2 + \sigma^{\mp}_{\tau_o\,j}{}^2\right)}{4} + \sigma^{\mp}_{t_t\,k}{}^2} \tag{14}$$

DATA

The average uncertainty range of each measured factor is shown in Table 2 for the peak calculation methods and the threshold calculation methods. The negative values indicate the uncertainty range less than the mean; the positive values indicate the uncertainty range greater than the mean. The uncertainty of measured factors are determined from propagation of measurement uncertainty. The measured true thickness, sound path, repetition, sampling, feature arrival, and velocity uncertainty values are assumed symmetric; the measured offset, thickness, and thickness error uncertainty values are allowed to be asymmetric. Some of the factors are not measured, but rather determined from the weighted censored relative likelihood method analysis; these non-measured factors and allowed to be asymmetric. The values in Table 2 are not an inclusive range among all measurements, but rather an average range to compare the typical uncertainty magnitude among factors.

The thickness error uncertainty will vary among calculation methods as displayed in Fig. 4a for an accurate and precise calculation method and Fig. 4b for a relatively imprecise method. The relative likelihood contour plot for the imprecise method from Fig. 4b is shown in Fig. 5. Three cumulative distribution function plots for the imprecise method are shown in Fig. 6; the thickness error measurement mean and associated asymmetric measurement uncertainty confidence limits, the maximum likelihood SEV model fit, the most likely (mean) value μ, the 95% upper confidence limit a_{95}, and the 95% lower confidence limit a_{05} are shown in Fig. 6a; a sample of 8 distribution models from the set of location scale parameters on the relatively likelihood 95% confidence region perimeter to demonstrate the simulation of potential distribution models are shown in 6b; the complete set of potential distribution models and the associated 95% upper confidence limit $a_{95/95}$ and 95% lower confidence limit $a_{05/05}$ are shown in Fig. 6c.

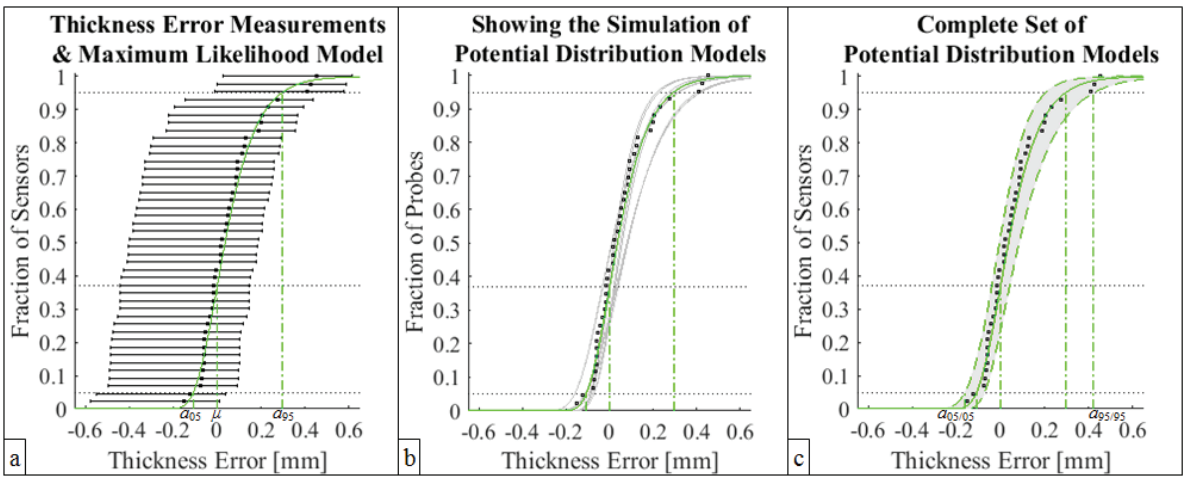

FIGURE 6. Three cumulative distribution function plots for the relatively imprecise measurement method are shown. Plot a) includes the thickness error measurement point and associated asymmetric uncertainty confidence limits. Plot b) includes a sampling from the set of location scale parameters on the relatively likelihood 95% confidence region perimeter. Plot c) includes the complete set of potential distribution models and the associated 95% upper confidence limit $a_{95/95}$ and 95% lower confidence limit $a_{05/05}$.

RESULTS AND ANALYSIS

Four metrics can be considered to compare the accuracy and precision among various calculation methods: the upper confidence limit $\left[a_{95/95_j} = t_{e_j} + \sigma^{+}_{t_{e_j}}\right]$ corresponding to over-reporting of the thickness, the lower confidence limit $\left[a_{05/05_j} = t_{e_j} - \sigma^{-}_{t_{e_j}}\right]$ corresponding to under-reporting of the thickness, the average confidence limit $\left[\frac{1}{2}\left(a_{95/95_j} + a_{05/05_j}\right)\right]$, as well as the maximum confidence limit $\left[\max\left(\left|a_{95/95_j}\right|, \left|a_{05/05_j}\right|\right)\right]$. For a symmetric logistic distribution, all four metrics provide equivalent information, but for asymmetric largest and smallest extreme value distributions, the distinction between metrics is of interest. The thickness error confidence limits for each of the 87 calculation methods are organized by measurement category in Fig. 7a for the maximum confidence limit, and in Fig. 7b for the upper and lower confidence limits.

In general, the first threshold methods are more precise and accurate, the peak and peak threshold methods are less precise, and the mean threshold methods are the least precise. The mean threshold methods relative lack of precision is exacerbated as the maximum confidence limits are upper confidence limits indicating a greater tendency for over-reporting of the thickness as opposed to a more conservative under-reporting of the thickness. Neither the voltage measurement nor the voltage threshold appear to have a significant influence on measurement accuracy and precision.

CONCLUSIONS

This paper proposed a weighted censored relative likelihood method to capture asymmetric measurement uncertainty as applied to a sol-gel ultrasonic thickness structural health monitoring measurement system. The upper and lower confidence limits of measurements collected on a flat calibration block over a short time period at ambient temperature were presented for 87 simple thickness calculation methods as a baseline. Future work could involve measurements in more extreme environments to quantify the potential decrease in performance (increase in measurement uncertainty) at elevated temperatures, for rough back-wall surfaces, and for system degradation over time. In addition, various pitch-catch configurations and more robust thickness calculation methods could be considered.

ACKNOWLEDGMENTS

This work supported by BP Products North America and Applus RTD Technological Center in the Netherlands.

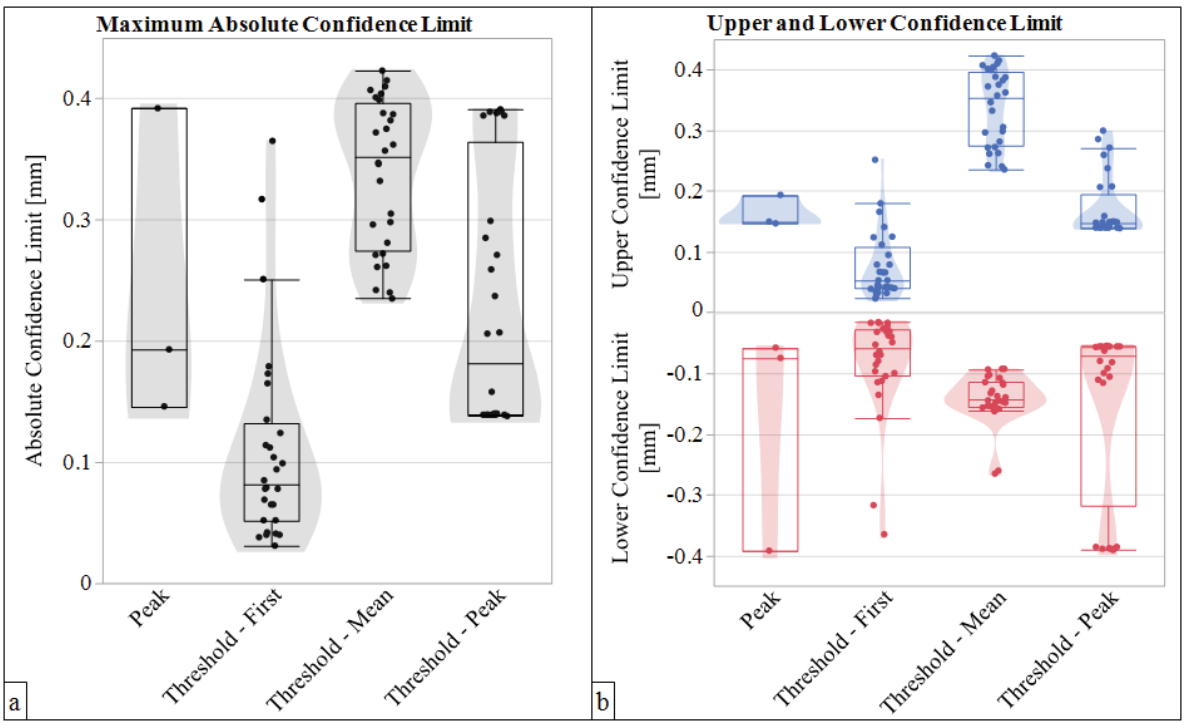

FIGURE 7. The a) thickness error absolute maximum confidence limit, and b) thickness error upper and lower confidence limit for each of the 87 calculation methods grouped by category are shown.

REFERENCES

1 F. Ropital, Materials and Corrosion **60**, 495–500 (2009).
2 W. Qing, Petroleum Technology Quarterly **Q4**, 35–43 (2010).
3 E. Slavcheva, B. Shone, and A. Turnbull, British Corrosion Journal **34**, 125–131 (1999).
4 X. Q. Wu, H. M. Jing, Y. G. Zheng, Z. M. Yao, and W. Ke, Journal of Materials Science **39**, 975–985 (2004).
5 M. Kobayashi and C. K. Jen, "Transducers for non-destructive evaluation at high temperatures," in *Ultrasonic Transducers: Materials and Design for Sensors, Actuators and Medical Applications*, edited by K. Nakamura (Woodhead Publishing Limited, Cambridge, 2012), pp. 408–443.
6 M. Kobayashi, C.-K. Jen, J. Bussiere, and K.-T. Wu, NDT & E International **42**, 157–161 (2009).
7 D. A. Barrow, T. E. Petroff, and M. Sayer, U.S. Patent No. 5,585,136 (12 December 1996).
8 K. Matthies, *Thickness Measurement with Ultrasound*, 1st ed. (DGZfp German Society of Nondestructive Testing, Berlin, 1998).
9 J. Krautkramer and H. Krautkramer, *Ultrasonic Testing of Materials* (Springer-Verlag, Berlin, 1990).
10 D. Ensminger and L. J. Bond, *Ultrasonics fundamentals, technologies, and applications* (CRC Press, Boca Raton, 2011).
11 D. E. Bray and R. K. Stanley, *Nondestructive Evaluation: A Tool in Design, Manufacturing, and Service* (CRC Press - Taylor & Francis Group, Boca Raton, 1997).
12 B. Barshan, Measurement Science and Technology **11** (2000).
13 A. J. C. Jarvis and F. B. Cegla, Journal of the Acoustical Society of America **132**, 1325–1335 (2012).
14 D. Benstock, F. B. Cegla, and M. Stone, Journal of the Acoustical Society of America **136**, 3028–3039 (2014).
15 H. Ku, Journal of Research of the National Bureau of Standards, Section C: Engineering and Instrumentation **70C**, 263–273 (1966).
16 B. N. Taylor and C. E. Kuyatt, United States Department of Commerce Technology Administration - National Institute of Standards and Technology - Physics Laboratory - Guidelines for Evaluating and Expressing the Uncertainty of NIST Measurement Results (1994).

17 W. Q. Meeker and L. A. Escobar, *Statistical Methods for Reliability Data* (John Wiley & Sons, New York, 1998).
18 C. Annis, Department of Defense Handbook - Nondestructive Evaluation System Reliability Assessment - MIL-HDBK-1823A (7 April 2009).
19 T. J. Eason, L. J. Bond, and M. G. Lozev, "Ultrasonic thickness structural health monitoring photoelastic visualization and measurement accuracy for internal pipe corrosion," in *Proc. SPIE 9439, Smart Materials and Nondestructive Evaluation for Energy Systems*, edited by N. G. Meyendorf (International Society for Optics and Photonics, San Diego, 2015) p. 94390M.
20 S. B. Vardeman and C.-S. Lee, IEEE Transactions on Instrumentation and Measurement **54**, 409–414 (2005).
21 S. Liu and W. Q. Meeker, Technometrics **57**, 164–179 (2015).
22 T. J. Eason, L. J. Bond, and M. G. Lozev, "Structural health monitoring of localized internal corrosion in high temperature piping for oil industry," in *AIP Conf. Proc., 41st Annual Review of Progress in Quantitative Nondestructive Evaluation: Volume 34*, edited by D. E. Chimenti and L. J. Bond (AIP Publishing LLC, Boise, 2015), pp. 863–873.
23 L. Svilainis, "Review of high resolution time of flight estimation techniques for ultrasonic signals," in *International Conference NDT* (Telford, 2012).
24 A. R. Selfridge, IEEE Transactions on Sonics and Ultrasonics **32**, 381–394 (1985).